



저작자표시-비영리-변경금지 2.0 대한민국

이용자는 아래의 조건을 따르는 경우에 한하여 자유롭게

- 이 저작물을 복제, 배포, 전송, 전시, 공연 및 방송할 수 있습니다.

다음과 같은 조건을 따라야 합니다:



저작자표시. 귀하는 원저작자를 표시하여야 합니다.



비영리. 귀하는 이 저작물을 영리 목적으로 이용할 수 없습니다.



변경금지. 귀하는 이 저작물을 개작, 변형 또는 가공할 수 없습니다.

- 귀하는, 이 저작물의 재이용이나 배포의 경우, 이 저작물에 적용된 이용허락조건을 명확하게 나타내어야 합니다.
- 저작권자로부터 별도의 허가를 받으면 이러한 조건들은 적용되지 않습니다.

저작권법에 따른 이용자의 권리는 위의 내용에 의하여 영향을 받지 않습니다.

이것은 [이용허락규약\(Legal Code\)](#)을 이해하기 쉽게 요약한 것입니다.

[Disclaimer](#)

공학석사학위논문

**방향 전환, 도약 각도 조절,
자세 교정이 가능한 점핑 로봇**

**A Jumping Robot Capable of Steering,
Adjusting the Take-Off Angle, and Self-Righting**

2019 년 2 월

서울대학교 대학원

기계항공공학부

임 소 정

Abstract

A Jumping Robot Capable of Steering, Adjusting the Take-Off Angle, and Self-Righting

Sojung Yim

Department of Mechanical and Aerospace Engineering

The Graduate School

Seoul National University

Jumping enables the robot to overcome obstacles that are larger than its own size. In order to reach the desired location with only jumping, the jumping robots integrated with additional functions – steering, adjusting the take-off angle, and self-righting – have been developed to expand the reachable range of the robot. Design to reduce mass is required as the integration of additional functions increases the mass of the robot and reduces the jumping performance. In this thesis, a jumping robot capable of steering, adjusting the take-off angle, and self-righting is proposed with the design of actuator and mechanism sharing to minimize the jumping performance degradation. The robot, with a mass of 70.1 g jumps up to 1.02 m in vertical height, and 1.28 m in horizontal distance. It can change the jumping height and distance by adjusting the take-off angle from 40°

to 91.9°. The robot can jump in all directions, and it can reach farther through multiple jumps. A dynamic model is established to predict the behavior of the robot and plan the jumping trajectory not only for jumping without slip but also for jumping with slip. The design method to implement more functions than the number of actuators can be applied to design other small-scale robots. This robot can be deployed to unstructured environments to perform tasks such as search and rescue, reconnaissance, and exploration.

Keywords : Mobile robot, Jumping robot, Multi-functional jumping robot, Mechanism sharing, Actuator sharing

Student Number : 2017-29144

Contents

Abstract	i
Contents	iii
List of Tables.....	v
List of Figures	vi
Chapter 1. Introduction.....	1
1.1. Motivation.....	1
1.2. Research Objectives and Contributions	3
1.3. Research Overview	6
Chapter 2. Design.....	7
2.1. Jumping.....	8
2.2. Steering	10
2.3. Take-off Angle Adjustment	12
2.4. Self-Righting	13
2.5. Integration	16
Chapter 3. Analysis.....	19
3.1. Dynamic Modeling.....	19
3.2. Simulated Results.....	24
3.3. Jumping Trajectory Planning	33

Chapter 4. Result.....	35
4.1. Performance	35
4.2. Demonstration.....	40
Chapter 5. Conclusion	46
Bibliography	49
국문 초록	53

List of Tables

Table 1.1 Comparison of various multi-functional jumping robots.....	4
Table 2.1 Mass budget of functions	17

List of Figures

Figure 1.1	The omnidirectional jumper prototype	5
Figure 2.1	Definitions of the (a) axes and (b) part names	7
Figure 2.2	Jumping mechanism. (a) 3D CAD view of the jumping/steering gearbox and (b) conceptual diagram of the mechanism. Rotating the head motor in clockwise stores the energy and rotating the motor in counterclockwise releases the energy.	10
Figure 2.3	Steering mechanism. (a) 3D CAD view of the jumping/steering gearbox and steering wheel. (b) Rotating the motor in counterclockwise steers the robot.	11
Figure 2.4	Conceptual diagram of take-off angle adjusting mechanism. (a) Initial posture when the bottom of the foot makes contact with the ground and the body angle is zero. (b) Rotating the foot motor in the clockwise increase the body angle. (c) Rotating the motor in the clockwise decreases the body angle.	13
Figure 2.5	Conceptual diagram of self-righting depending on landing postures. The front and back side landings	

mean the foot and the righting linkage are located under the body, respectively. (a) Front side landing. First, shorten the length between the CoM and the foot joint, and then upright. (b) Back side landing. The righting linkage pushes against the ground to force the robot into an upright position.15

Figure 2.6 Control scheme of the robot17

Figure 3.1 Dynamic model of the robot and its coordinate. The model consists of four masses (p_1, p_6, p_7, p_8), four links (p_2, p_3, p_4, p_5), and four joints. Left side indicates xz -plane view, and right side indicates yz -plane view.....21

Figure 3.2 Simulated results of relation between body angle and (a) take-off angle and (b) take-off velocity. The Red section refers to jumping without slip, the blue section refers to jumping transition from no-slip to slip and the green section refers to jumping with slip from initial.....26

Figure 3.3 Simulated results of (a) kinematic values of θ_1 and y_1 (b) velocity of the CoM (c) reaction forces and (d) energy when the body angle is 60° 29

Figure 3.4 Simulated results of (a) kinematic values of θ_1 and

	y_1 (b) velocity of the CoM (c) reaction forces and (d) energy when the body angle is 50°	30
Figure 3.5	Simulated results of (a) kinematic values of θ_1 and y_1 (b) velocity of the CoM (c) reaction forces and (d) energy when the body angle is 40°	31
Figure 3.6	Comparison of high-speed images and visualized simulated results of the robot's motion from initial to take-off about the body angle of (a) 60° , (b) 50° , and (c) 40° Black dots, blue diamonds, and red circles mean the position of the joint, masses or links, and CoM of the robot, respectively	32
Figure 3.7	Take-off angle and velocity in yz-plane. (y_d, z_d) is the coordinate of the target position.....	34
Figure 4.1	Jumping trajectories in six different body angles.....	36
Figure 4.2	Experimental results of the comparison of the body angle and the take-off angle.	37
Figure 4.3	Sequences of steering. It takes 59 s for one revolution.	39
Figure 4.4	Sequences of self-righting depending on the landing postures. (a) Front side landing takes 53 s to right. (b) Back side landing takes 58 s to right.	39

Figure 4.5	Jumping trajectories on the terrain with obstacles. Three jumps are performed to overcome two obstacles. The obstacles have heights of 0.75 m and 0.15 m, and distance of 0.15 m and 0.6 m.	41
Figure 4.6	Definition of the distance to the obstacle D and height of the obstacle H	43
Figure 4.7	Measured angle of the robot from the IMU and measured distance from the distance sensor while recognizing the (a) distance to the obstacle and (b) height of the obstacle	44
Figure 4.8	Jumping trajectories of overcoming two different obstacles by sensing an obstacle with the distance sensor and the IMU. The height of the red obstacle is 0.45 m, the blue obstacle is 0.6 m, and the distance to both obstacles are about 0.25 m.....	45

Chapter 1. Introduction

1.1. Motivation

Small-scale mobile robots have the advantage of exploring confined environments that are inaccessible to people or large robots [1]. The robot can pass through narrow gaps and go inside to search or perform tasks. However, the smaller size of the robot, the larger relative size of the environment in which the robot moves [2]. Therefore, the small-scale robots need the ability to overcome obstacles in order to move in an unstructured environment.

Moving through jumping, the robot can overcome obstacles that are relatively larger than its body length. Therefore, various jumping robots have been developed [3–10], and the robots have shown good jumping performance. Kovac et al. [3] designed the miniature 7 g jumping robot that jumps 27 times the body length, Noh et al. [4] designed the flea inspired jumping robot that jumps a height that is 30 times larger than its body length, and Zaitsev et al. [5] designed the locust-inspired miniature jumping robot that jumps 25 times its body length.

In order for jumping robots to be used in practical situations such as planetary exploration, reconnaissance, search and rescue, the robot should be able to move to the desired location. There are two major methods for the jumping robot to increase the reachable region

and reach the desired location. First one is adding another locomotion mode to jumping locomotion, such as jump-crawling [11]. Jump-crawling robot can crawl toward a desired location, and when it encounters obstacles that cannot be overcome by crawling, the robot can jump over the obstacles. The second one is integrating additional functions into jumping locomotion. Steering enables the robot to jump to the desired direction. By adjusting the take-off angle, the jumping height and jumping distance can be changed. If the robot cannot reach the desired location within a single jump, the robot can reach there with multiple jumps through self-righting.

For this reason, jumping robots integrated with the aforementioned functions have been developed [12–17]. MSU jumper [12] can jump, steer, and self-right by one motor, however, it has fixed take-off angle. The third generation of JPL robot [13] can jump, steer, and adjust the take-off angle, and the self-righting function is not integrated. A bio-inspired jumping robot [14] can jump by one motor, and steer, adjust the take-off angle and self-right by the other motor, however, it has limited adjusting range of the take-off angle and steering. Table 1.1 compares various multi-functional jumping robot. To our knowledge, three additional functions – continuously steering, continuously adjusting the take-off angle, and self-righting – have not been fully integrated into a single small-scale jumping robot.

Integrating mechanisms of additional functions into the jumping mechanism increases mass, and the jumping performance reduces as

the jumping height is inversely proportional to its mass when the stored energy is the same. Researchers have studied integration strategies [12, 13, 18]. Multimo-Bat [18] integrates jumping and gliding by sharing the actuation and structural components required for each locomotion mode to increase the mobility of the robot with minimal performance degradation. Likewise, mechanism design to integrate additional functions while minimizing the jumping performance degradation is necessary.

1.2. Research Objectives and Contributions

The main research objective is to present a jumping robot, named omnidirectional jumper [19], capable of steering, self-righting, and take-off angle adjustment as illustrated in Fig. 1.1. To reduce the mass of the robot, the robot is designed by sharing the mechanisms and actuators that operate each function. Sharing some components of the mechanism for each function reduces the total number of components that make up the robot, compared to when the mechanism of each function is composed of independent components, which is one method to reduce the mass. Therefore, only two motors are integrated into the robot to perform jumping, steering, adjusting the take-off angle, and self-righting.

Table 1.1. Comparison of various multi-functional jumping robots

Robot	Mass (g)	Size (mm)	Jumping height (m)	Jumping distance (m)	Normalized jumping height (m)	Steering	Take-off angle adjustment	Self-righting	Actuation
MSU Jumper [12]	23.5	65	0.87	0.89	0.93	YES	NO	YES	1 motor
Bio-inspired jumping robot [14]	154	120	0.88	0.30	0.90	YES (360° in 14 steps)	YES (80.33 ~ 86.92°)	YES	2 motors
JPL second generation robot [13]	1300	150	0.90	2.0	1.08	YES	NO	YES	N/A
JPL third generation robot [13]	N/A	N/A	0.30	N/A	N/A	YES	YES (N/A)	NO	N/A
Steerable miniature jumping robot [15]	14	180	0.62	0.21	0.66	YES	NO	YES	2 motors
Omnidirectional jumper [19]	70.1	190	1.02	-0.15	1.02	YES	YES (40 ~ 91.9°)	YES	2 motors

The dynamics of the jumping robot is analyzed to estimate the motion of the robot. Most of the previous researches analyze the jumping motion assuming that there is no slip [4, 14, 16]. In this thesis, the dynamic model deals with both cases of jumping without slip and jumping with slip because slip can occur at low take-off angle. This makes it possible to compare dynamics with and without slip.

To sum up, the contributions of this thesis are (1) development of a jumping robot capable of steering, adjusting the take-off angle, and self-righting, (2) dynamic modeling of the jumping robot for both cases of jumping without slip and with slip, (3) demonstrating the ability to overcome obstacles for using the robot in unstructured environments.

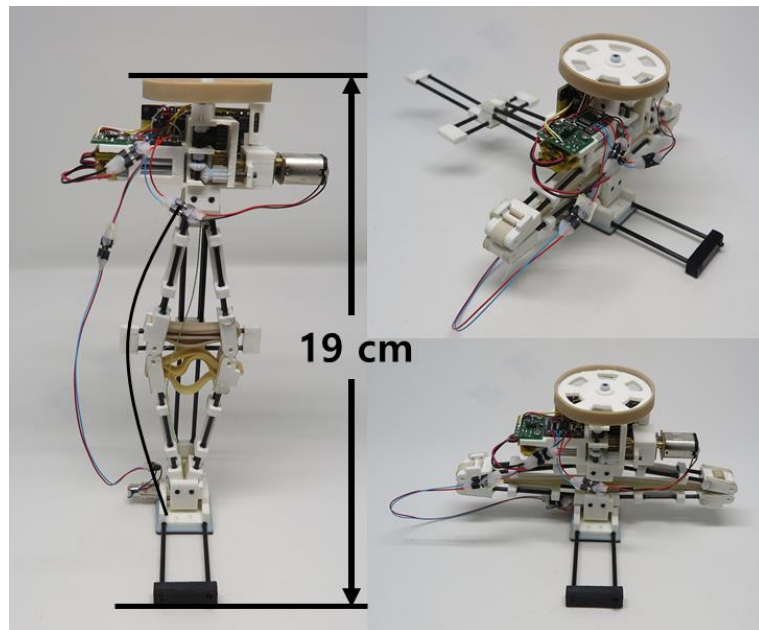


Figure 1.1 The omnidirectional jumper prototype

1.3. Research Overview

The thesis is organized as follows. Design section explains the mechanism of each function and the methods how the actuators and mechanisms are shared to operate each function. Analysis section presents the dynamic modeling of the jumping robot to better understand the motion of the jumping robot. The simulated results from the dynamic model are used to plan the jumping trajectory of the robot. Result section describes the performance of the jumping robot. Also, two demonstrations are proposed that show the robot's ability to move by remote control or overcome an obstacle autonomously through sensing an obstacle.

The jumping robot has a length of about 190 mm and a mass of about 70 g. The maximum jumping height is 1.02 m, the maximum jumping distance is 1.28 m, and the robot can change the jumping height and distance by adjusting the take-off angle. The robot can jump in all direction by steering, and the robot can jump multiple times by self-righting.

Chapter 2. Design

The jumping robot shown in Fig. 2.1 performs four functions; jumping, steering, take-off angle adjustment, and self-righting. Integration of additional functions into the jumping mechanism increase the total mass of the robot. As the mass increases, the jumping height decreases. Therefore, an important issue in designing the robot is to reduce the jumping performance degradation due to the additional mass, and our approach is to share mechanisms and actuators that perform each function.

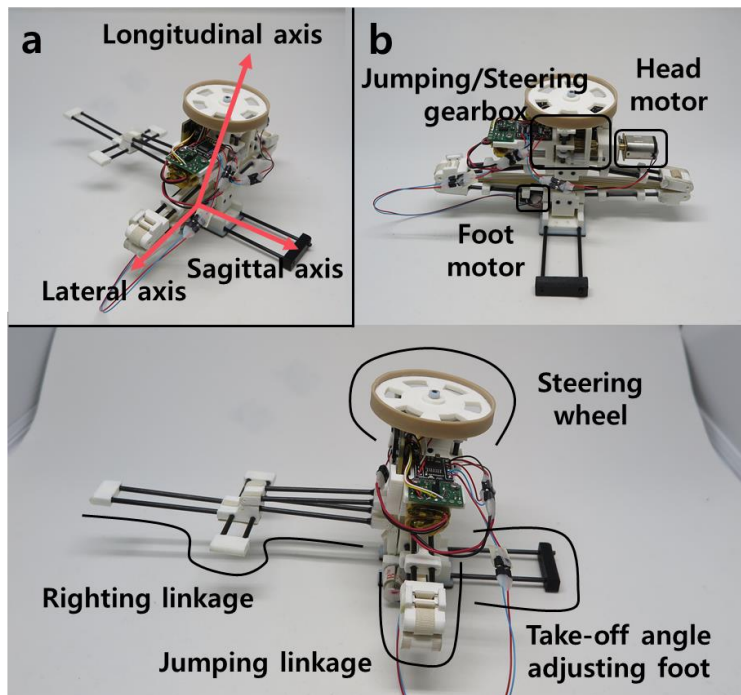


Figure 2.1 Definitions of the (a) axes and (b) part names

The robot consists of two motors and various parts for implementing four functions. For jumping, there are a jumping linkage, a jumping/steering gearbox, and a head motor. A steering wheel is attached to the top of the gearbox. A foot motor and a take-off angle adjusting foot are located at the bottom of the jumping linkage. The righting linkage is connected to the jumping linkage. Detail descriptions of each function are provided below.

2.1. Jumping

The jumping mechanism consists of a rhombus-shaped four-bar linkage named as jumping linkage, latex bands for energy storage, jumping/steering gearbox, and the head motor as shown in Fig. 2.2. This jumping mechanism was developed in the previous research [11]. In a rhombus-shaped four-bar linkage, the latex bands are fixed to one pair of facing joints, and a cord passes the other pair of joints. One end of the cord is fixed to the winding pulley gear, and the other end is fixed to the bottom of the robot. The latex bands stretch when the four-bar linkage become compressed.

The jumping/steering gearbox is designed to perform jumping and steering with a single motor. The gearbox consists of an actuating gear which is fixed to the motor, a traveling gear which moves along the groove while rotating along the rotation direction of the motor, and a winding pulley gear and a steering gear that operate

each function. The traveling gear engages with or disengages from the winding pulley gear or steering gear depending on the rotation direction of the motor.

Jumping utilize the engagement relation of the actuating gear, the traveling gear, and the winding pulley gear. To store energy, the traveling gear should engage with the winding pulley gear to transfer the motor torque to the winding pulley gear. When the motor rotates in a clockwise direction as shown in Fig. 2.2(b), the traveling gear engages with the winding pulley gear, and all three gear rotates together. Rotation of the winding pulley gear winds the cord, and the distance between the two joints passing through the cord decreases, so the jumping linkage become compressed. As a result, the latex band stretches and stores energy. When the motor stops, all gears stop rotating and maintain their position, therefore, the stored energy is maintained. To release energy, the winding pulley gear should be free to rotate so that the wound cord can be released. When the motor rotates in a counterclockwise direction, the traveling gear disengages from the winding pulley gear, and the motor torque is no longer transmitted to the winding pulley gear. Then, the cord is released, and the linkage is restored to its original shape by the restoring force of the latex bands. Then, the energy stored in the latex band is released, and the robot jumps.

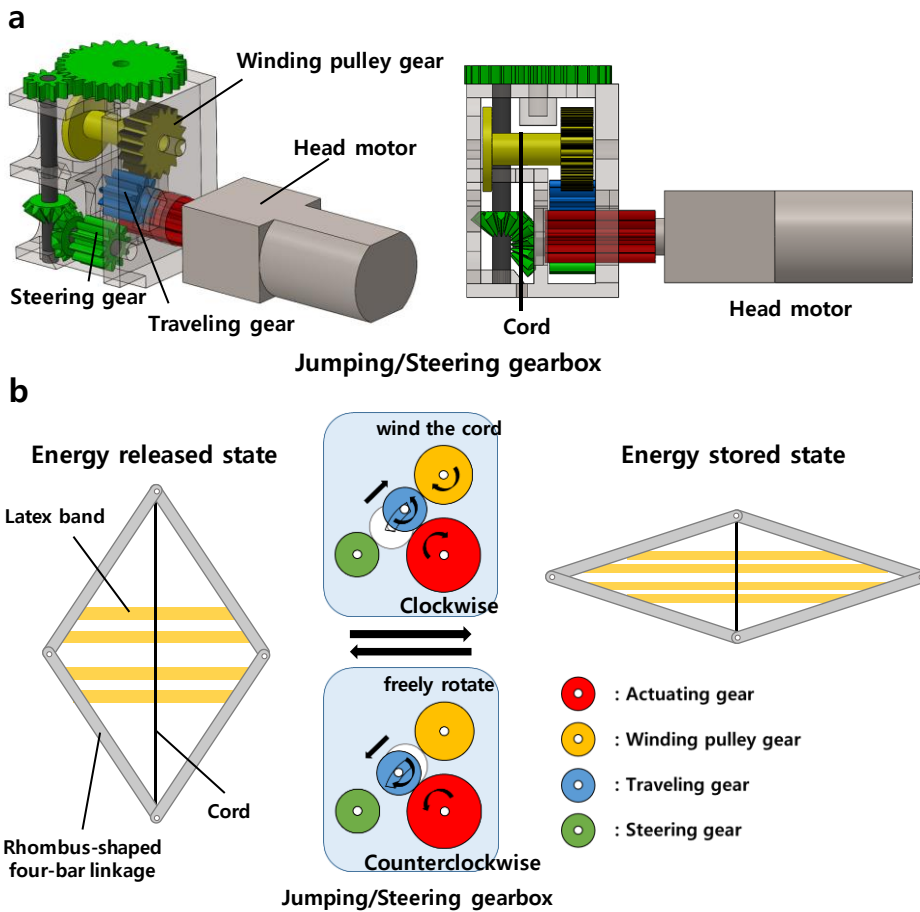


Figure 2.2 Jumping mechanism. (a) 3D CAD view of the jumping/steering gearbox and (b) conceptual diagram of the mechanism. Rotating the head motor in clockwise stores the energy and rotating the motor in counterclockwise releases the energy.

2.2. Steering

Steering changes the jumping direction, so the robot can jump in the desired direction. The steering mechanism consists of the

steering wheel, jumping/steering gearbox, and the head motor as illustrated in Fig. 2.3. Rotating the steering wheel while the wheel is in contact with the ground changes the direction of the robot.

The steering wheel is rotated by the head motor and the jumping/steering gearbox. When the motor rotates in the counterclockwise direction, the traveling gear moves along the groove and engages with the steering gear as shown in Fig. 2.3(b). Then, the rotation of the motor transfers to the rotation of the steering wheel.

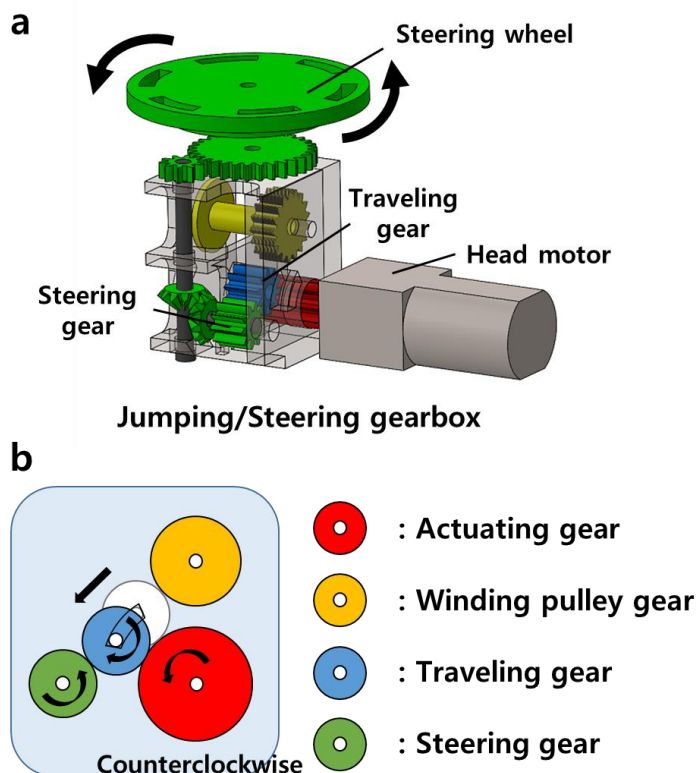


Figure 2.3 Steering mechanism. (a) 3D CAD view of the jumping/steering gearbox and steering wheel. (b) Rotating the motor in counterclockwise steers the robot

2.3. Take-off Angle Adjustment

Adjusting the take-off angle changes the jumping height and the jumping distance. The take-off angle can be adjusted by changing the angle between the ground and the longitudinal axis of the robot before take-off. The angle is defined as the body angle illustrated in Fig. 2.4(b). The foot motor, a torsional spring, and the take-off angle adjusting foot are included in the take-off angle adjustment mechanism to change the body angle. The motor with a pulley is fixed to the foot, and one end of the cord is wound on this pulley and the other end of the cord is fixed to the bottom of the main body. Each end of the torsional spring is fixed to the main body and the foot. To prevent the robot from falling down, the foot is designed with appropriate length so that the projection of the center of mass (CoM) to the ground always be located inside the foot area.

Rotating the motor in the counterclockwise direction increases the body angle by winding the cord, and the rotating the motor in the clockwise direction unwinds the cord and decreases the body angle as shown in Fig. 2.4(b) and (c).

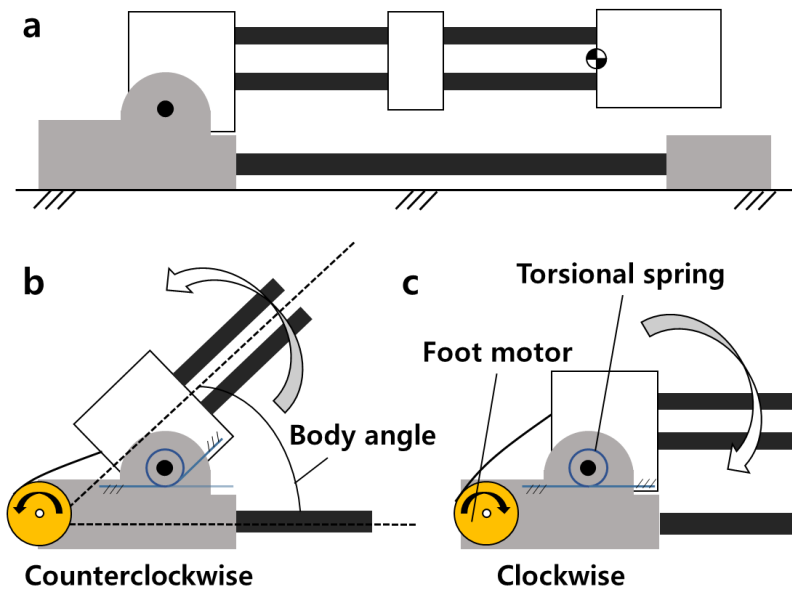


Figure 2.4 Conceptual diagram of take-off angle adjusting mechanism. (a) Initial posture when the bottom of the foot makes contact with the ground and the body angle is zero. (b) Rotating the foot motor in the counterclockwise increase the body angle. (c) Rotating the motor in the clockwise decreases the body angle.

2.4. Self-Righting

Self-righting is required to allow repeated jumps even if the robot lands on the ground in any posture. In the case of this robot, the body shape is designed to land only in two postures. Flat body shape and initially flexed foot allow only front or back side landing. Front side landing denotes the landing posture when the foot is beneath the body, and the back side landing denotes the landing posture when the righting linkage is beneath the body. Self-righting

mechanisms of both landing cases are implemented without extra actuators. Descriptions of both landing cases are given below.

2.4.1. Front Side Landing

Self-righting of front side landing is identical with the situation of the take-off angle adjustment, as the bottom side of the foot is in contact with the ground. Therefore, the robot can be upright by operating the foot motor. As there is a limit torque of the motor to raise up the entire body, energy is first stored to reduce the length between the foot joint and the CoM and then upright as shown in Fig. 2.5(a).

2.4.2. Back Side Landing

Self-righting of back side landing is implemented by adding only two links. The two links are connected by joints, and the ends of both links are connected to the top and bottom of the jumping linkage so that the motion of the righting linkage interconnect with the motion of the jumping linkage. When the jumping linkage is compressed, the mid joint of the righting linkage protrudes perpendicularly to the plane of the jumping linkage and it pushes against the ground as shown in Fig. 2.5(b). In order for this linkage not to interfere with

other functions, the linkage must be fully folded when the latex bands are in the unstretched state and completely folded when the jumping linkage is entirely compressed. By actuating the head motor, energy storage and righting are performed simultaneously.

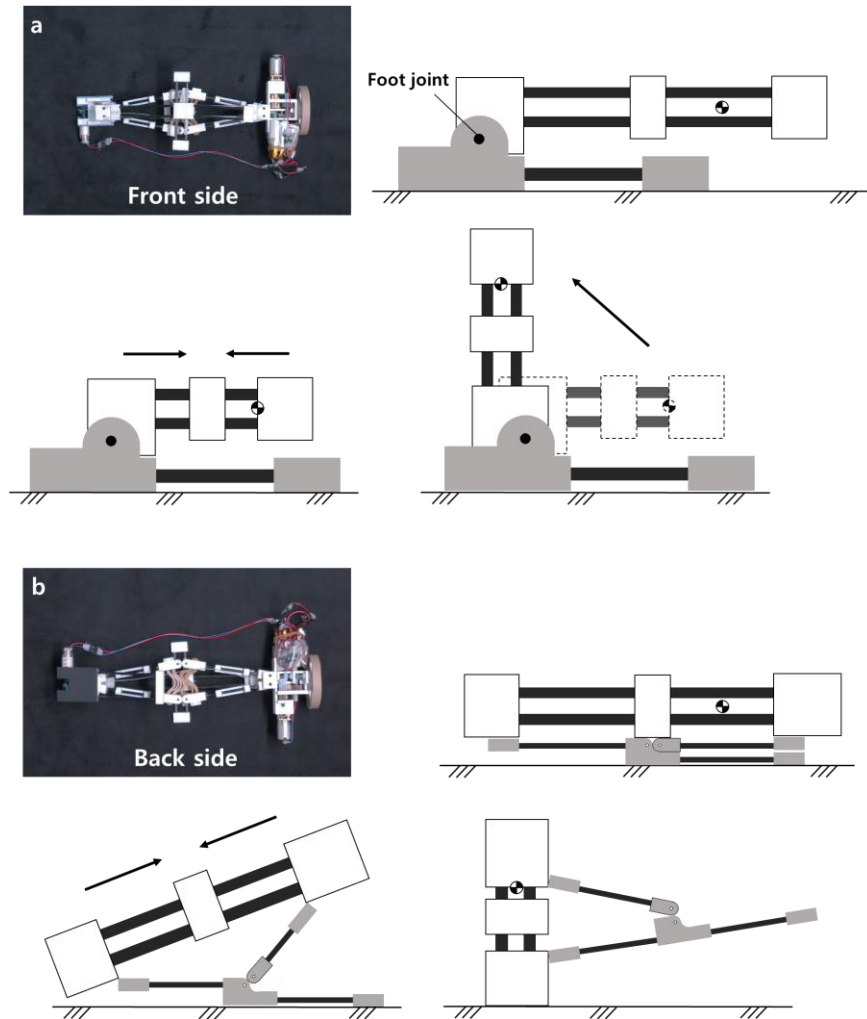


Figure 2.5 Conceptual diagram of self-righting depending on landing postures. The front and back side landings mean the foot and the righting linkage are located under the body, respectively. (a) Front side landing. First, shorten the length between the CoM and the foot joint, and then upright. (b) Back side landing. The righting linkage pushes against the ground to force the robot into an upright position.

2.5. Integration

2.5.1. The Prototype of the Jumping Robot

The body of the robot is made of 3D printed parts and carbon rods for a light mass. A DC motor (Pololu 1000:1 gear ratio) is used as the head motor and the other DC motor (D&J LCP06–A03V–0700) is used as the foot motor. The motors are controlled by the Intel Curie–based board (DFrobot Curie Nano) and a motor driver (DFrobot Thumbnail Sized DC Motor Driver 2x1.5A). The board uses Bluetooth Low Energy (BLE) for communication. Also, a distance sensor (Pololu VL53L0X) is integrated, and the control board contains 9–axis IMU. The power is given by two 170 mAh LiPo batteries with 3.7V. The overall control scheme is illustrated in Fig. 2.6.

The mass of the entire robot is 70.1 g and the mass budget of each function is described in Table 2.1. The size of the robot is 190 mm height \times 85 mm width \times 45 mm depth when the energy is released, and 90 mm height \times 135 mm width \times 140 mm depth when the energy is stored. The length from bottom to CoM is 113 mm when energy released, and 27 mm when energy stored.

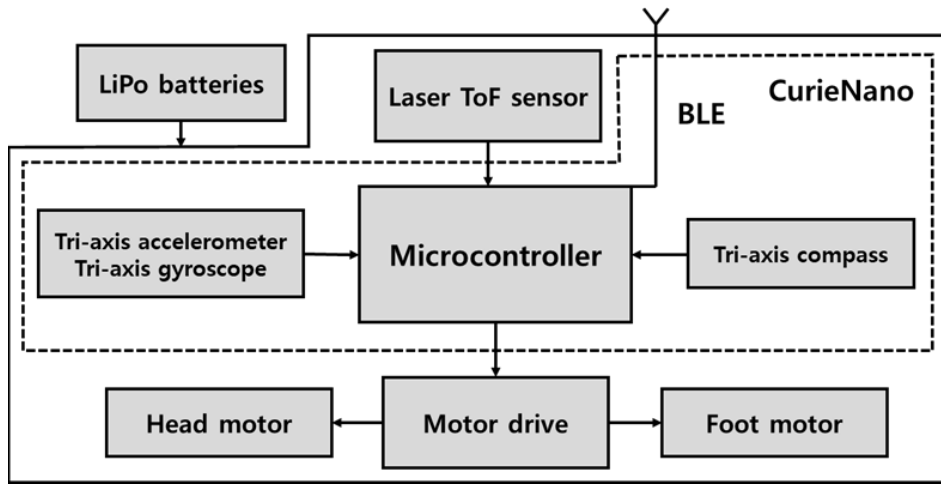


Figure 2.6 Control scheme of the robot

Table 2.1 Mass budget of functions

Functions	Mass (g)	Portion (%)
Jumping mechanism	37.4	53
Take-off angle adjusting mechanism	8.60	12.3
Steering mechanism	3.30	4.7
Self-righting mechanism	3.96	5.6
Sensor, Control board, LiPo batteries	16.9	24.1
Total	70.1	100

2.5.2. Operating Sequences

The motor that performs each function is shared, therefore, there are predetermined operating sequences for repeated jumps. After the robot lands, the robot first steers, and it is performed before energy storage. To maintain the energy stored, the motor should be stopped to prevent the winding pulley gear being released, therefore, the head motor cannot be operated for steering after storing energy. After steering to the desired direction, the robot stores energy. Depending on the landing posture, righting is performed at the same time as energy storing or by using the foot motor after completing energy storage. After righting, the desired body angle is set using the foot motor. Then the robot releases the energy and it jumps. Repeated jumps are possible by repeating the previous steps and a summary of the sequences is as follows.

- 1) Landing on the front side: steer, energy store, right, adjust the take-off angle, and jump
- 2) Landing on the back side: steer, energy store and right simultaneously, adjust the take-off angle, and jump

Chapter 3. Analysis

3.1. Dynamic Modeling

A Dynamic model enables the estimation of the behavior of the jumping robot. To estimate the robot's jumping trajectory, it is necessary to know the take-off angle and the take-off velocity. The configurable variable to adjust the take-off angle and velocity is the body angle. Therefore, the take-off angle and velocity with respect to the body angle are calculated based on the model.

The jumping dynamics is analyzed based on the Lagrangian formulation [11, 14]. The body angle can be adjusted between zero to 90 degrees. In a range of low body angles, slip might occur due to insufficient friction. Therefore, the dynamics is analyzed by dividing it into two models, one not including slip and the other including slip.

The jumping robot is modeled with four links, four masses, and four revolute joints illustrated in Fig. 3.1. The positions of the CoM of links and masses are described as follows:

$$p_1 = \begin{bmatrix} x_1 \\ y_1 \\ z_1 \end{bmatrix} \quad (3.1)$$

$$p_2 = \begin{bmatrix} x_1 + (L/2) \sin(\theta_1/2) \\ y_1 + d_{1,y} - d \sin \theta_3 + (L/2) \cos(\theta_1/2) \cos \theta_3 \\ z_1 + d_{1,z} + d \cos \theta_3 + (L/2) \cos(\theta_1/2) \sin \theta_3 \end{bmatrix} \quad (3.2)$$

$$p_3 = \begin{bmatrix} x_1 - (L/2) \cos(\theta_1 + \theta_2) \\ y_1 + d_{1,y} - d \sin \theta_3 + (L/2) \sin(\theta_1 + \theta_2) \cos \theta_3 \\ z_1 + d_{1,z} + d \cos \theta_3 + (L/2) \sin(\theta_1 + \theta_2) \sin \theta_3 \end{bmatrix} \quad (3.3)$$

$$p_4 = \begin{bmatrix} x_1 + (L/2) \sin(\theta_1/2) \\ y_1 + d_{1,y} - d \sin \theta_3 + (3L/2) \cos(\theta_1/2) \cos \theta_3 \\ z_1 + d_{1,z} + d \cos \theta_3 + (3L/2) \cos(\theta_1/2) \sin \theta_3 \end{bmatrix} \quad (3.4)$$

$$p_5 = \begin{bmatrix} x_1 - (L/2) \sin(\theta_1/2) \\ y_1 + d_{1,y} - d \sin \theta_3 + (3L/2) \cos(\theta_1/2) \cos \theta_3 \\ z_1 + d_{1,z} + d \cos \theta_3 + (3L/2) \cos(\theta_1/2) \sin \theta_3 \end{bmatrix} \quad (3.5)$$

$$p_6 = \begin{bmatrix} x_1 + d_{10,x} \\ y_1 + d_{1,y} - d \sin \theta_3 + 2L \cos(\theta_1/2) \cos \theta_3 \\ \quad + d_{10,y} \cos \theta_3 - d_{10,z} \sin \theta_3 \\ z_1 + d_{1,z} + d \cos \theta_3 + 2L \cos(\theta_1/2) \sin \theta_3 \\ \quad + d_{10,y} \sin \theta_3 + d_{10,z} \cos \theta_3 \end{bmatrix} \quad (3.6)$$

$$p_7 = \begin{bmatrix} x_1 + d_{11,x} \\ y_1 + d_{1,y} - d \sin \theta_3 + 2L \cos(\theta_1/2) \cos \theta_3 \\ \quad + d_{11,y} \cos \theta_3 - d_{11,z} \sin \theta_3 \\ z_1 + d_{1,z} + d \cos \theta_3 + 2L \cos(\theta_1/2) \sin \theta_3 \\ \quad + d_{11,y} \sin \theta_3 + d_{11,z} \cos \theta_3 \end{bmatrix} \quad (3.7)$$

$$p_8 = \begin{bmatrix} x_1 + d_{12,x} \\ y_1 + d_{1,y} - d \sin \theta_3 + 2L \cos(\theta_1/2) \cos \theta_3 \\ \quad + d_{12,y} \cos \theta_3 - d_{12,z} \sin \theta_3 \\ z_1 + d_{1,z} + d \cos \theta_3 + 2L \cos(\theta_1/2) \sin \theta_3 \\ \quad + d_{12,y} \sin \theta_3 + d_{12,z} \cos \theta_3 \end{bmatrix} \quad (3.8)$$

where p_i is the position of each link or mass, L is the length of four bar linkage, and d_i is the distance to each mass.

The dynamics is solved numerically with respect to one generalized coordinate, θ_1 , which is the included angle of the four-bar linkage. The initial conditions are

$$\theta_1(0) = 168^\circ, \quad \dot{\theta}_1(0) = 0 \quad (3.9)$$

Substituting the solved $\theta_1(t)$ into equations representing the

$$m_{robot}a_{robot,z}(t) = \sum_{i=1}^8 m_i a_{i,z}(t) = V(t) - \sum_{i=1}^8 m_i g \quad (3.11)$$

m_{robot} is the total mass of the robot, a_{robot} is the acceleration of the robot' s CoM, m_i is the mass of each link, a_i is the acceleration of each link, and g is the gravitational acceleration. Comparing the H_y and the multiplication of μ_s and V , if

$$H_y > \mu_s V \quad (3.12)$$

then slip occurs. In this case, the sliding friction should be considered in the equation of motion.

The jumping dynamics with friction force is calculated based on the Udwadia–Kalaba equation [20]. To include slip in the model, the position of the CoM of each link or mass is described with three generalized coordinates, θ_1 , y_1 , and z_1 , and one constraint is applied as (3.13) not to move in z -direction before take-off.

$$z_1 - c = 0 \quad (c = \text{constant}) \quad (3.13)$$

The unconstrained equation of motion is given by

$$M\ddot{x} = Q \quad (3.14)$$

where

$$M = \begin{bmatrix} m_{11} & m_{12} & m_{13} \\ m_{12} & m_{22} & 0 \\ m_{13} & 0 & m_{33} \end{bmatrix}, \quad \ddot{x} = \begin{bmatrix} \ddot{\theta}_1 \\ \ddot{y}_1 \\ \ddot{z}_1 \end{bmatrix}, \quad Q = \begin{bmatrix} q_1 \\ q_2 \\ q_3 \end{bmatrix} \quad (3.15)$$

The matrix A and vector b are calculated by differentiating the constraint (3.13) twice times with respect to time

$$[0 \quad 0 \quad 1] \begin{bmatrix} \ddot{\theta}_1 \\ \ddot{y}_1 \\ \ddot{z}_1 \end{bmatrix} = 0 \quad (3.16)$$

so that $A = [0 \quad 0 \quad 1]$, and $b = [0]$. The force of this constraint Q_i^c is

calculated as

$$Q_i^C = M^{1/2}(AM^{-1/2})^+(b - AM^{-1}Q) \quad (3.17)$$

where superscript + of a matrix is the Moore–Penrose inverse of the matrix. Including the Coulomb friction with a coefficient of friction μ_k and the magnitude of the constraint force $|Q_i^C|$, a non–ideal constraint by kinetic friction is described by

$$C = -\mu_k \begin{bmatrix} 0 \\ 1 \\ 0 \end{bmatrix} |Q_i^C| = \mu_k \begin{bmatrix} 0 \\ 1 \\ 0 \end{bmatrix} |Q_i^C| \quad (3.18)$$

The constraint force due to this non–ideal constraint Q_{ni}^C is given by

$$Q_{ni}^C = C - M^{1/2}(AM^{-1/2})^+AM^{-1}C \quad (3.19)$$

The total constraint force Q^C is

$$Q^C = Q_i^C + Q_{ni}^C \quad (3.20)$$

and the equation of motion of the constrained system can be expressed as

$$M\ddot{x} = Q + Q^C, \quad x(0) = x_0, \quad \dot{x}(0) = \dot{x}_0 \quad (3.21)$$

The equation of motion is solved numerically with the initial conditions

$$\begin{aligned} \theta_1(0) &= 168^\circ, \quad \dot{\theta}_1(0) = 0 \\ y_1(0) &= 19.6 \text{ mm}, \quad \dot{y}_1(0) = 0 \\ z_1(0) &= 6.2 \text{ mm}, \quad \dot{z}_1(0) = 0 \end{aligned} \quad (3.22)$$

when slip occurs from the starting point. If condition (3.12) is satisfied in the middle of take–off process, the time t_s that

$$H_y(t_s) - \mu_s V(t_s) = 0 \quad (3.23)$$

is found, and the values of θ_1 , y_1 , and z_1 at time t_s become the initial conditions for solving equation of motion with slip.

Take-off occurs when the vertical reaction force $V(t)$ becomes zero.

$$V(t_f) = \sum_{i=1}^8 m_i a_{i,z}(t_f) + \sum_{i=1}^8 m_i g = 0 \quad (3.24)$$

After finding the time t_f at which the vertical reaction force becomes zero and calculating the kinematics of each mass at the take-off time, the take-off angle and velocity can be calculated.

$$m_{robot} v_{robot,y}^f = \sum_{i=1}^8 m_i v_{i,y}^f \quad (3.25)$$

$$m_{robot} v_{robot,z}^f = \sum_{i=1}^8 m_i v_{i,z}^f \quad (3.26)$$

$$\varphi_f = \tan^{-1}\left(\frac{v_{robot,z}^f}{v_{robot,y}^f}\right) \quad (3.27)$$

v_{robot} is the velocity of the robot's CoM, superscript f means the values at take-off, and φ_f is the take-off angle.

3.2. Simulated Results

The relations between the body angle and the take-off angle and velocity obtained from the model are illustrated in Fig. 3.2. The motion of the jumping robot can be divided into three cases depending on the body angle. The first case is that the robot jumps without slip, with body angles between about 54° and 90° , which is highlighted with a red section in Fig. 3.2. The second case is that the robot

initiates jumping without slip and it starts slip in the middle, with body angles between about 46° and 53° , which is highlighted with a blue section in Fig. 3.2. The last case is that the robot jumps with slip, with body angles between about 40° and 46° , which is illustrated with a green section in Fig. 3.2. The boundary angles at which changing the motion characteristics are determined from the static coefficient of friction and the reaction force profiles which depends on the design of the jumping linkage. Simulated results utilize the measured values of the kinetic coefficient of friction ($\mu_k = 0.43$) and the static coefficient of friction ($\mu_s = 0.69$) between the robot and the ground which were used in experiments.

When there is no slip, the take-off angle is the same as the body angle, and the take-off velocity is almost constant at different body angles. The origin of the body coordinate does not move in no slip case, so the longitudinal axis also does not move. The CoM of the robot moves along the longitudinal axis, therefore, the angle of the velocity vector with respect to the global coordinate is the same as the body angle. The take-off velocity is about at 4.5 m/s. There is no energy loss due to slip, so the energy stored in the latex bands is converted to kinetic energy with almost the same conversion efficiency.

When slip occurs during jumping, the take-off angle becomes larger than the body angle, and the take-off angle becomes smaller as the body angle decreases. When the robot applies a horizontal force to the ground greater than the maximum static friction force,

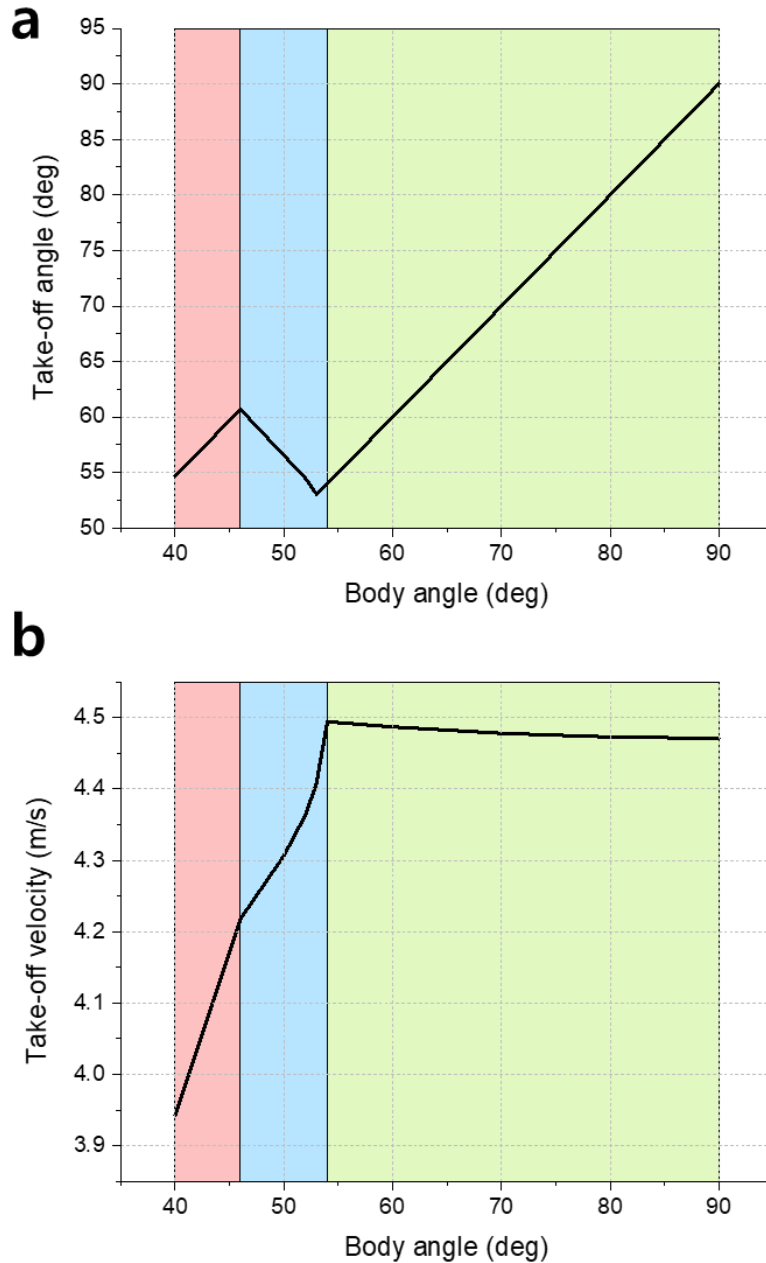


Figure 3.2 Simulated results of relation between body angle and (a) take-off angle and (b) take-off velocity. The red section refers to jumping without slip, the blue section refers to jumping transition from no-slip to slip and the green section refers to jumping with slip from initial.

slip occurs and the robot receives a horizontal reaction force only equal to the kinetic friction force. The robot cannot receive sufficient horizontal reaction force to avoid slip, so the horizontal component of the velocity is reduced. Therefore, the angle between the horizontal and vertical component of the velocity becomes larger. In other words, the CoM of the robot moves along the longitudinal axis, and the longitudinal axis moves in the $-Y$ direction in the global frame. Therefore, the angle of the vector connecting the position of the CoM of the initial point and the take-off point becomes larger than the body angle. Also, the smaller the body angle, the larger the magnitude of the horizontal force required to avoid slip. Because the difference between the force required to prevent slip and the kinetic friction force calculated by the vertical reaction force increases as the body angle becomes smaller, the bottom of the robot slides more. The take-off velocity decreases as the energy loss due to slip becomes larger.

Fig. 3.3 shows the simulated results with the body angle of 60° , which refers to jumping without slip. The horizontal component of the take-off velocity is 2.24 m/s, and the vertical component of the take-off velocity is 3.89 m/s, therefore, the take-off angle is 60.0° which is same as the body angle, and the take-off velocity is 4.49 m/s. Fig. 3.3(c) shows the reaction forces, and the horizontal component of the reaction force is smaller than the multiplication of static coefficient of friction and vertical component of the reaction force, which means slip does not occur. As shown in Fig. Fig. 3.3(d),

the total energy is conserved because there is no energy loss due to slip, and the amount of energy is 1.06 J.

Fig. 3.4 shows the simulated results with the body angle of 50° , which refers to jumping with a transition from no slip to slip. The horizontal component of the take-off velocity is 2.38 m/s, and the vertical component of the take-off velocity is 3.59 m/s, therefore, the take-off angle is 56.5° which is larger than the body angle, and the take-off velocity is 4.31 m/s. In Fig. 3.4(c), it can be seen that the reaction force profile changes when slip occurs and the equation of motion changes. As shown in Fig. Fig. 3.4(d), the total energy is conserved at 1.06 J until slip occurs, and 0.04 J of energy is reduced.

Fig. 3.5 shows the simulated results with the body angle of 40° , which refers to jumping with slip. The horizontal component of the take-off velocity is 2.28 m/s, and the vertical component of the take-off velocity is 3.22 m/s, therefore, the take-off angle is 54.7° , and the take-off velocity is 3.94 m/s. The initial energy is 1.06 J, and there is 0.11 J of energy loss due to slip, so the energy at take-off is 0.95 J.

Fig. 3.6 compares the visualized simulated results and the sequences of high-speed images of three cases of body angle. The bottom of the robot doesn't move in Fig. 3.6(a). As shown in Fig. 3.6(b), the bottom slides to $-y$ direction about 7 mm in simulation and 4.4 mm in the experiment. In Fig. 3.6(c), the bottom slides to $-y$ direction about 22 mm in simulation and 24 mm in the experiment. As the body angle decreases, the robot slides more distance.

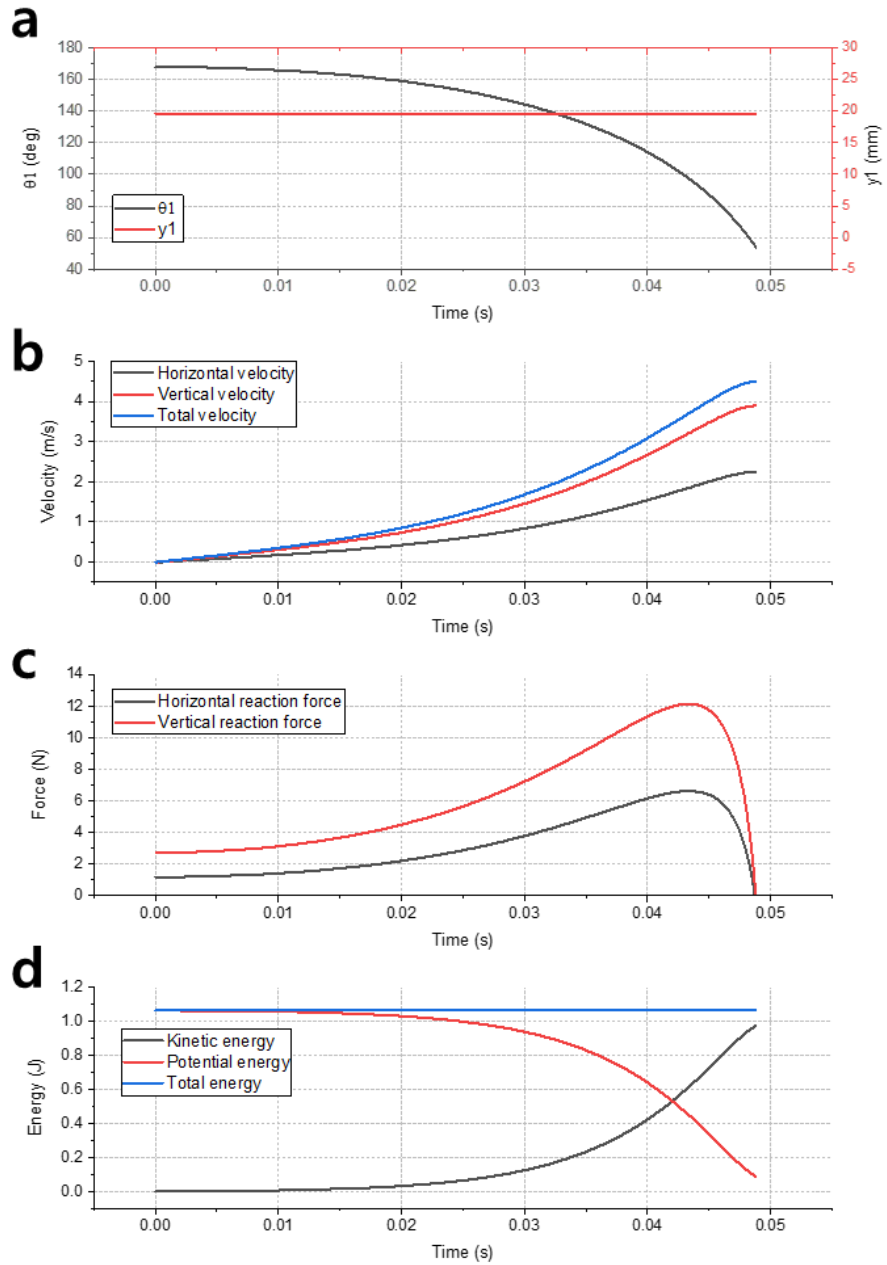


Figure 3.3 Simulated results of (a) kinematic values of θ_1 and y_1 (b) velocity of the CoM (c) reaction forces and (d) energy when the body angle is 60°

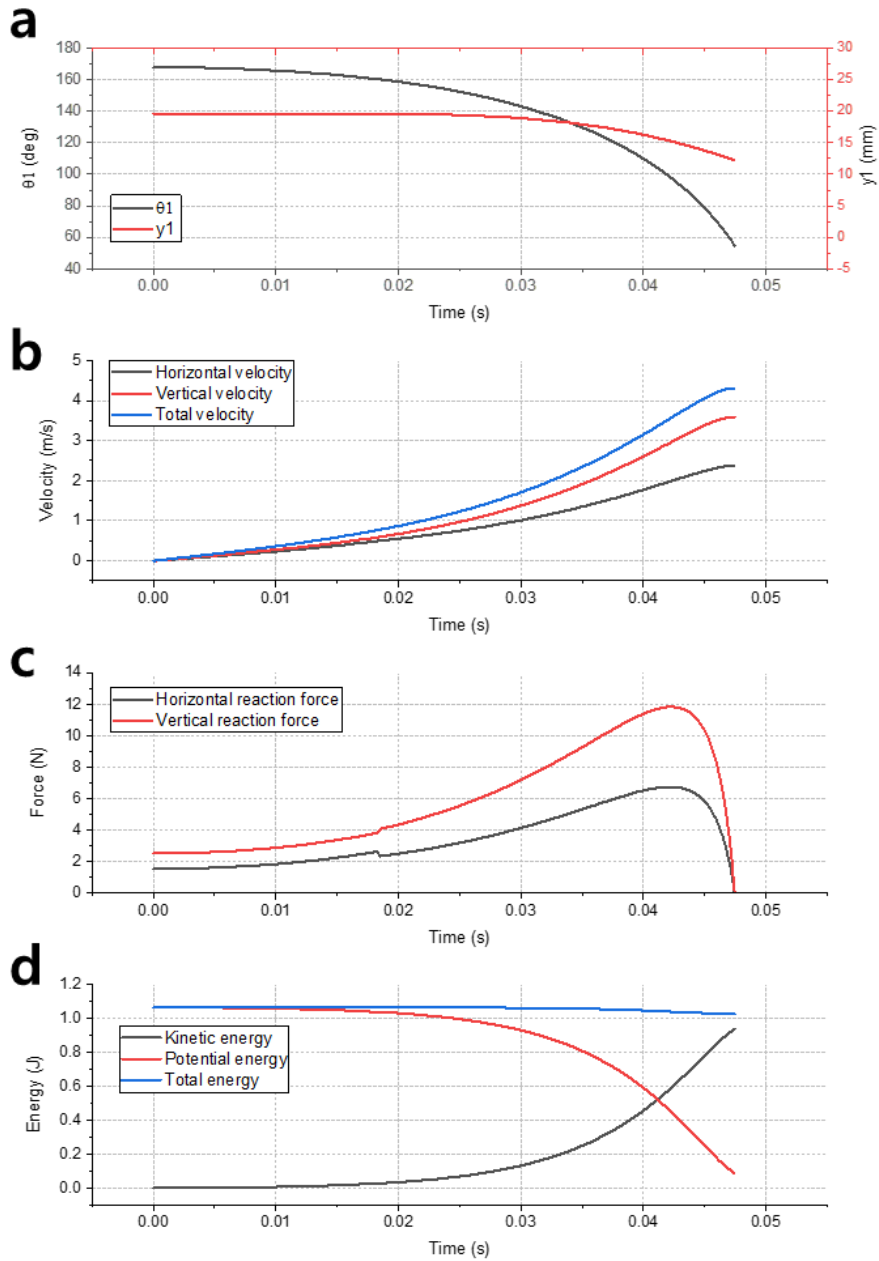


Figure 3.4 Simulated results of (a) kinematic values of θ_1 and y_1 (b) velocity of the CoM (c) reaction forces and (d) energy when the body angle is 50°

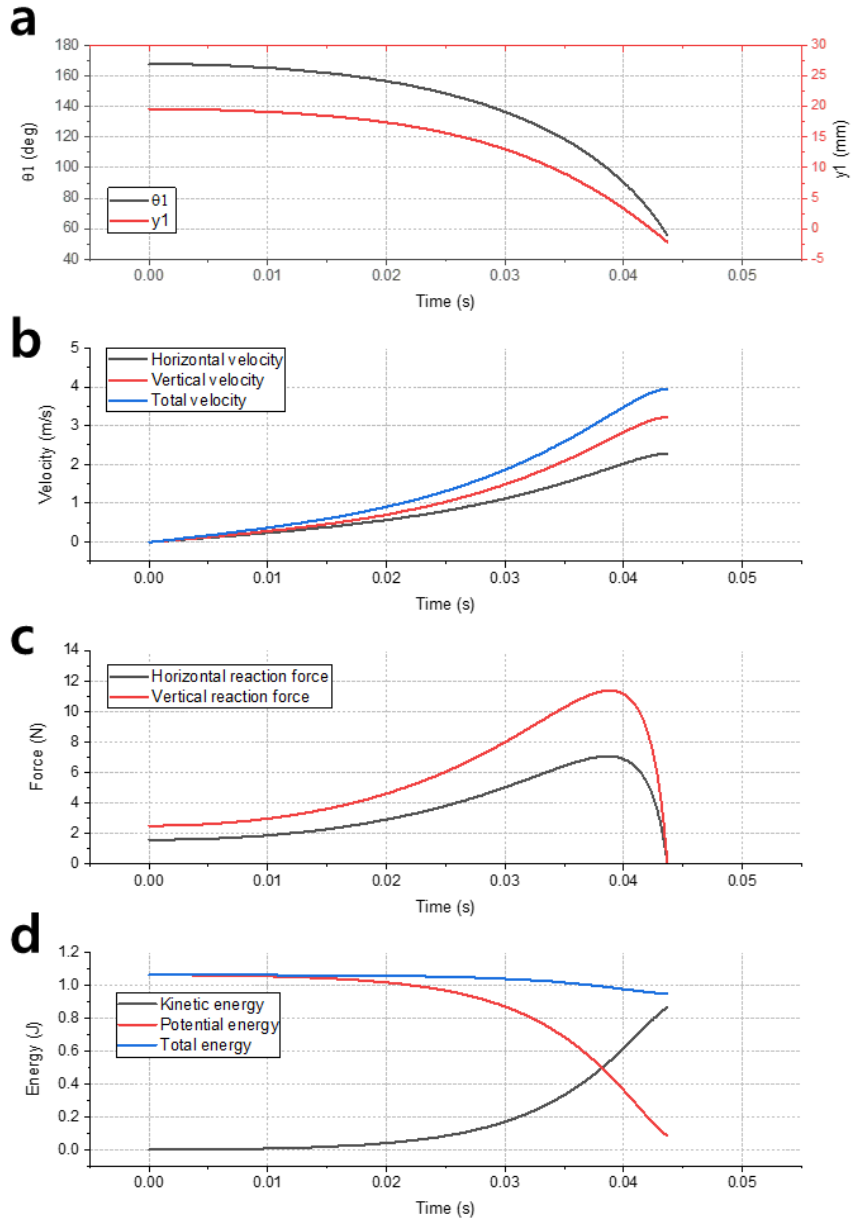


Figure 3.5 Simulated results of (a) kinematic values of θ_1 and y_1 (b) velocity of the CoM (c) reaction forces and (d) energy when the body angle is 40°

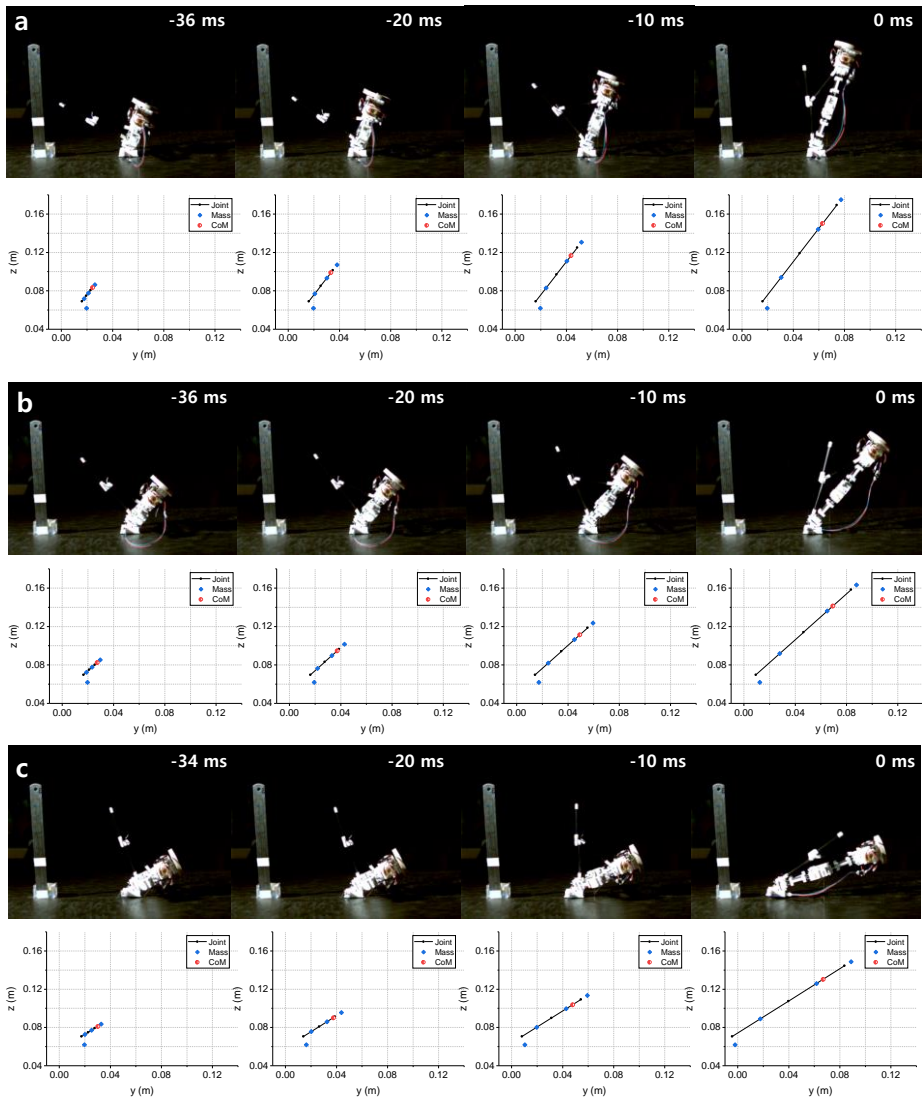


Figure 3.6 Comparison of high-speed images and visualized simulated results of the robot's motion from initial to take-off about the body angle of (a) 60° , (b) 50° , and (c) 40° . Black dots, blue diamonds, and red circles mean the position of the joint, masses or links, and CoM of the robot, respectively.

3.3. Jumping Trajectory Planning

The body angle that makes the trajectory of the robot through the desired point should be calculated. If the air drag is neglected for simplification, the robot would move along the parabolic path in the air. The parabolic equation in yz -plane is

$$z = \tan \varphi - \frac{g}{2v_0^2 \cos^2 \varphi} y^2 \quad (3.28)$$

when the robot takes-off with the angle of φ and the velocity of v_0 (Fig. 3.7).

In the case of jumping without slip, the body angles at which the robot passes the desired point (y_d, z_d) in the yz -plane can be calculated analytically. Because the body angle and the take-off angle are the same, and the take-off velocity is constant regardless of the body angle, the equation (3.28) can be used to derive the equation for φ , and it is same as the body angle θ_d . There are two parabolas passing one point, and two body angles for generating each parabola are

$$\begin{aligned} \theta_d &= \frac{1}{2}\alpha + \frac{1}{2}\sin^{-1}\left(\frac{z_d + gy_d^2/v_0^2}{\sqrt{y_d^2 + z_d^2}}\right) \\ \text{or } \theta_d &= \frac{1}{2}(\alpha + \pi) - \frac{1}{2}\sin^{-1}\left(\frac{z_d + gy_d^2/v_0^2}{\sqrt{y_d^2 + z_d^2}}\right) \end{aligned} \quad (3.29)$$

$$(\alpha = \tan^{-1}(z_d/y_d))$$

In the case of jumping with slip, the body angles are calculated numerically as the take-off angle and velocity are both dependent on

the body angle. Firstly, expressions of the relation between the body angle and the take-off angle ($\varphi = \varphi(\theta)$) and velocity ($v_0 = v_0(\theta)$) are obtained and substituted into the parabolic equation (3.28). The body angle that satisfying the equation (3.30) is calculated numerically.

$$z_d - \tan \varphi(\theta) + \frac{g}{2v_0(\theta)^2 \cos^2 \varphi(\theta)} y_d^2 = 0 \quad (3.30)$$

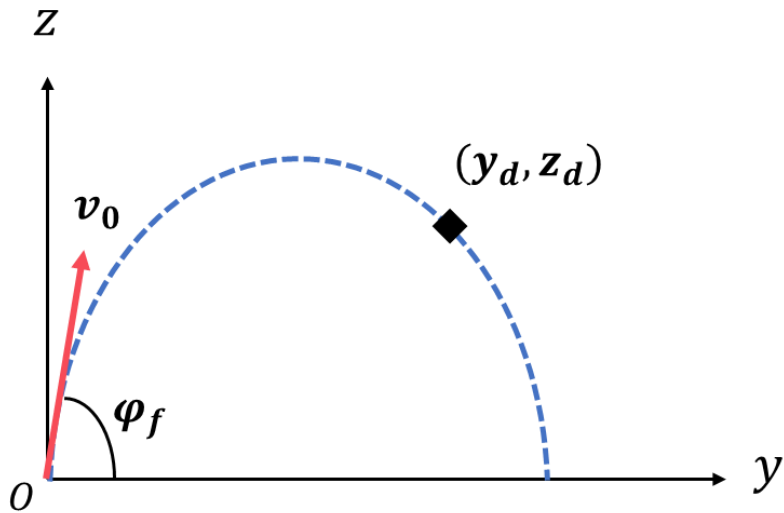


Figure 3.7 Take-off angle and velocity in yz -plane. (y_d, z_d) is the coordinate of the target position.

Chapter 4. Result

Some experiments are performed to test the performance of the jumping robot. The maximum jumping height and distance, trajectories for different body angles, steering and self-righting performance were examined. Jumping experiments were conducted on a flat ground. The jumping movements were recorded, and trajectories were obtained by the open source motion analysis software *Tracker* [21].

4.1. Performance

4.1.1. Front Side Landing

The maximum jumping height and jumping distance were measured to determine the range where the robot can reach in a single jump. Jumping performances were calculated as the average of three trials. The maximum jumping height was 1.02 m, which is about five times the body length at the take-off angle of 91.9° and the distance of 0.15 m. The maximum jumping distance was 1.28 m, which is about six times the body length at the take-off angle of 63.4° and the height of 0.75 m.

4.1.2. Take-off Angle Adjustment

The adjusting ranges of jumping height and distance were examined by adjusting the take-off angle through the body angle. Fig. 4.1 illustrate five different jumping trajectories with respect to the body angles. The robot can jump between 1.02 m and 0.75 m in height, and between 1.28 m and -0.15 m in distance.

The experimental result of relationship between the body angle and the take-off angle and velocity is shown in Fig. 4.2. There are some errors between the simulated and experimental results, and this might come from the motion of the righting linkage, which is not

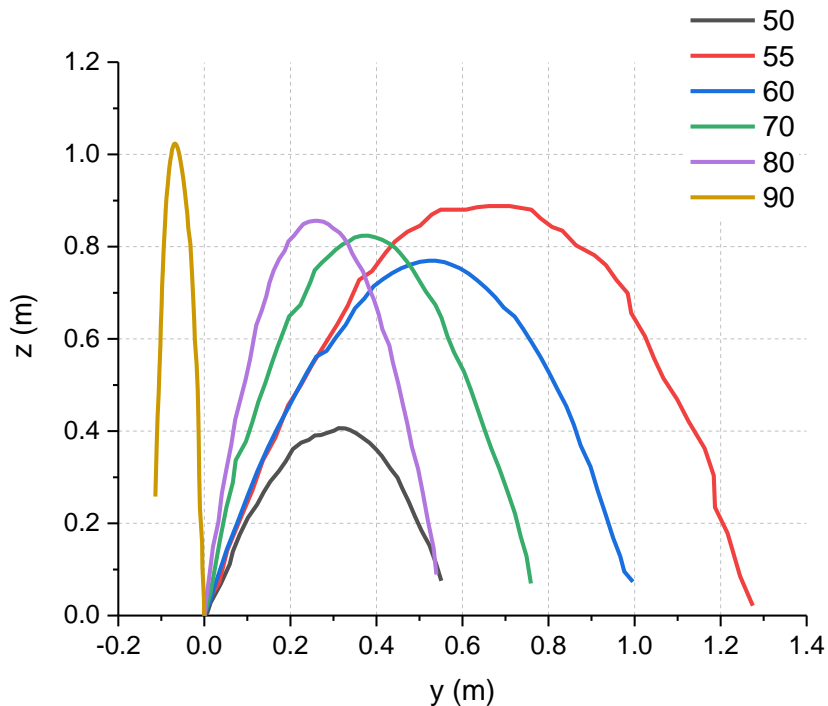


Figure 4.1 Jumping trajectories in six different body angles

included in the model. The righting linkage is connected perpendicularly to only one side of the jumping linkage. When the righting linkage becomes straight as the jumping linkage after the energy is released, the fast movement of the righting linkage generates impact to the jumping linkage. This impact makes the bending of the jumping linkage about x-axis and might affect the kinematics of the CoM at take-off.

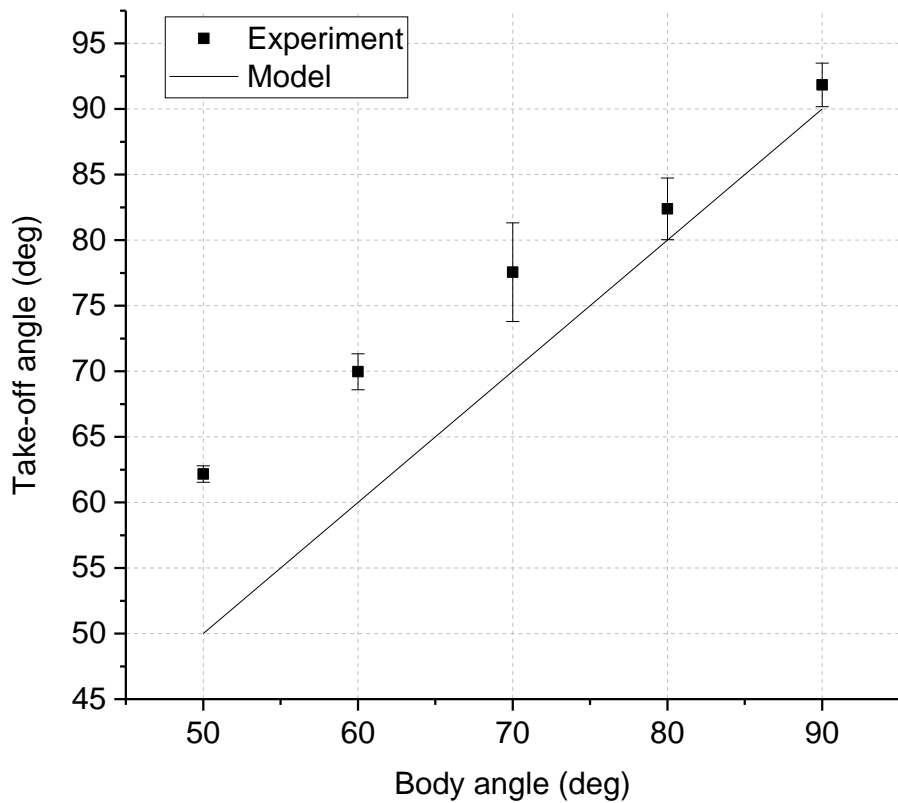


Figure 4.2 Experimental results of the comparison of the body angle and the take-off angle

4.1.3. Steering

The steering experiment is performed to test the steering mechanism and verify the robot's performance. Fig. 4.3 shows the sequences of steering, which can be continuously adjusted over a 360-degree range and it takes 59 s per revolution. As steering uses the counterclockwise rotation of the head motor, the robot can only steer clockwise.

4.1.4. Self-Righting

The self-righting experiment is conducted to check the self-righting mechanism and its performance. Fig. 4.4 shows the sequences of self-righting depending on the landing sides. In the case of the front side, energy is stored and the body is lifted using the foot motor, which takes 53 s. In the case of the back side, folding of the righting linkage when storing energy pushes the ground to upright the robot and it takes 58 s. Self-righting can be considered as not time-consuming because it works in parallel with energy-storing.

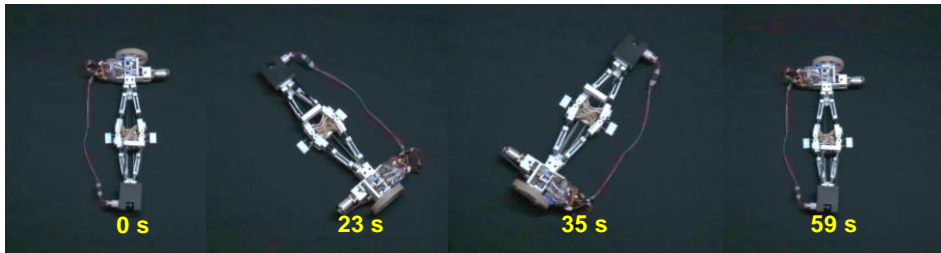


Figure 4.3 Sequences of steering. It takes 59 s for one revolution.

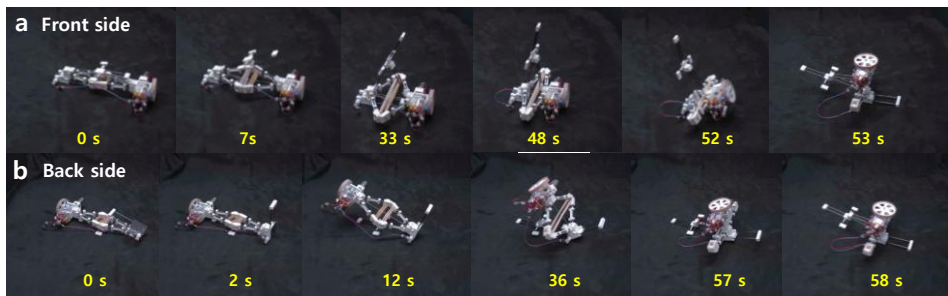


Figure 4.4 Sequences of self-righting depending on the landing postures. (a) Front side landing takes 53 s to right. (b) Back side landing takes 58 s to right.

4.2. Demonstration

4.2.1. Overcoming Obstacles Controlled by Human

A demonstration is performed to show that the robot can move to the target location in an environment with obstacles. After falling to the initial position at random, the robot reaches the final position passing through two obstacles of different heights and widths. The two obstacles are 75 cm, 15 cm, and 15 cm, 60 cm in height and width, respectively, and they are 90 cm apart. Fig. 4.5 shows the trajectory of the jumping robot; it reaches the final location through three jumps. The robot jumps with high take-off angle to jump over the first high and narrow barrier, and it jumps with low take-off angle to jump over the second low and long barrier. All four functions – jumping, adjusting the take-off angle, steering, and self-righting – are used for this demonstration.

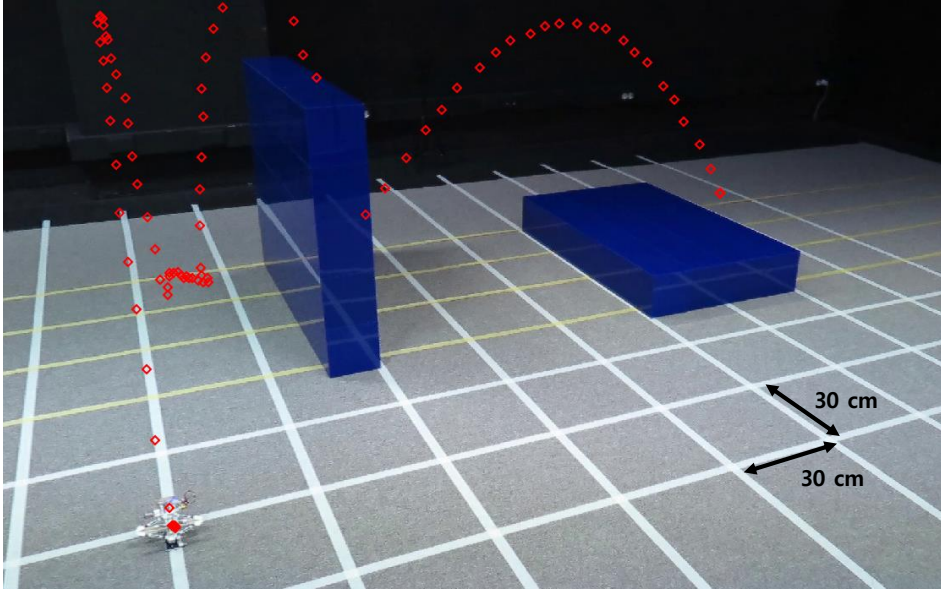


Figure 4.5 Jumping trajectories on the terrain with obstacles. Three jumps are performed to overcome two obstacles. The obstacles have heights of 0.75 m and 0.15 m, and distance of 0.15 m and 0.6 m.

4.2.2. Overcoming an Obstacle Autonomously

Another demonstration is performed to show that the robot can sense an obstacle and overcome it with an appropriate take-off angle. To overcome the obstacle successfully, the robot should know the distance to the obstacle and the height of the obstacle as shown in Fig. 4.6. The distance sensor and the IMU are used to measure the distance and height of the obstacle, and the robot calculates the desired take-off angle based on the measured values. It is assumed that the obstacle is a rectangular shape, and there are no other

objects closer to the obstacle, and the robot is driven on the flat ground.

The robot first measures the distance to the obstacle. To measure the distance, the robot finds the point where the distance measured from the sensor is minimum. Therefore, by measuring the distance while the robot steers one turn, the currently measured distance is compared to the previously measured distance and the angle of the point at the minimum distance θ_m is saved. After rotating one turn, the head motor is driven until the current angle becomes equal to the saved angle. Then, the robot stores the energy and measures the distance to the obstacles. Fig. 4.7 shows the angle measured by the IMU and the distance measured by distance sensor for the partial region while measuring the distance to the obstacle.

Then, the robot measures the height of the obstacle. The distance is measured while increasing the body angle of the robot. When the source of the distance sensor passes the edge of the obstacle, the measured distance increases sharply, and the robot saves the body angle of that point. Fig. 4.7 shows the measured angle and the distance while measuring the height of the obstacle. Using the saved body angle θ_s and the measured distance D , the robot calculates the height of the obstacle H as (4.1).

$$H = D \tan \theta_s \quad (4.1)$$

Based on the measured distance and height, the trajectory of the jumping robot to overcome the obstacle is determined. To ensure that the robot overcomes the obstacle, the desired point is specified as

$$y_d = D, \quad z_d = H' = H + BL \quad (4.2)$$

that the robot passes through the height H' calculated by adding the body length BL to the calculated height H at the measured distance D . By substituting (4.2) for y_d and z_d of the equation (3.29) or (3.30), the desired body angle is calculated. The foot motor is driven until the current angle becomes equal to the desired body angle.

Fig. 4.8 shows the jumping trajectories overcoming two different height of obstacles. The robot jumps with appropriate take-off angles according to the dimension of the obstacles that the robot measured.

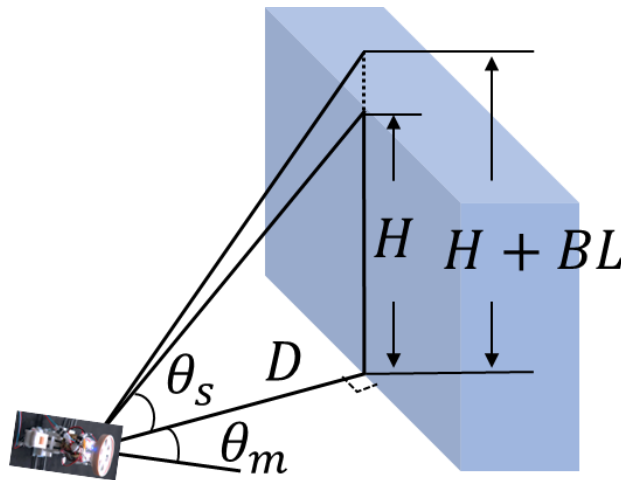


Figure 4.6 Definition of the distance to the obstacle D and height of the obstacle H

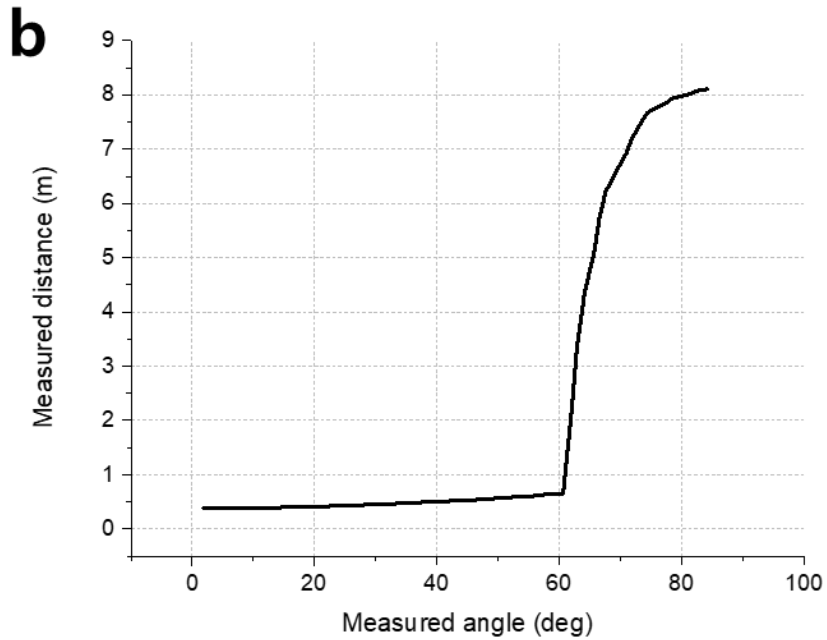
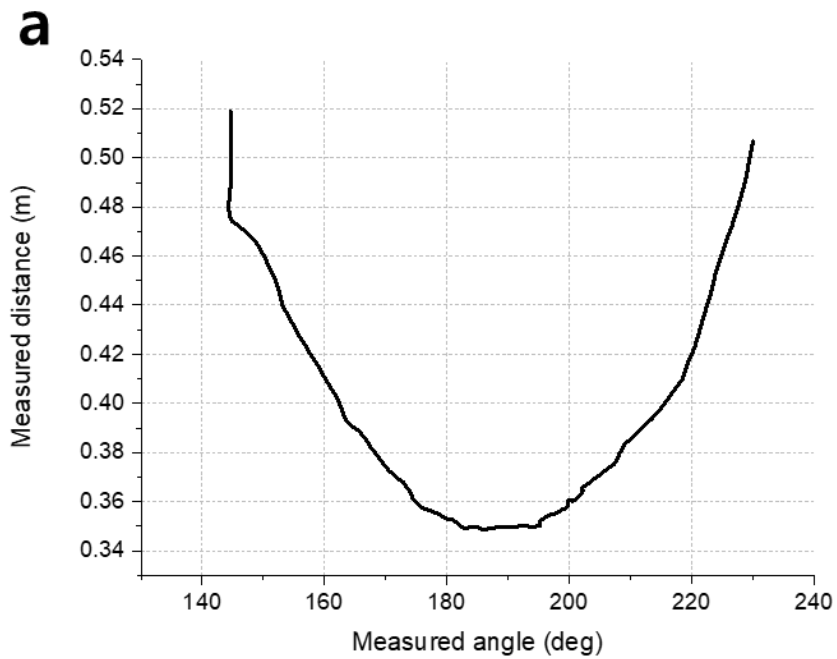


Figure 4.7 Measured angle of the robot from the IMU and measured distance from the distance sensor while recognizing the (a) distance to the obstacle and (b) height of the obstacle

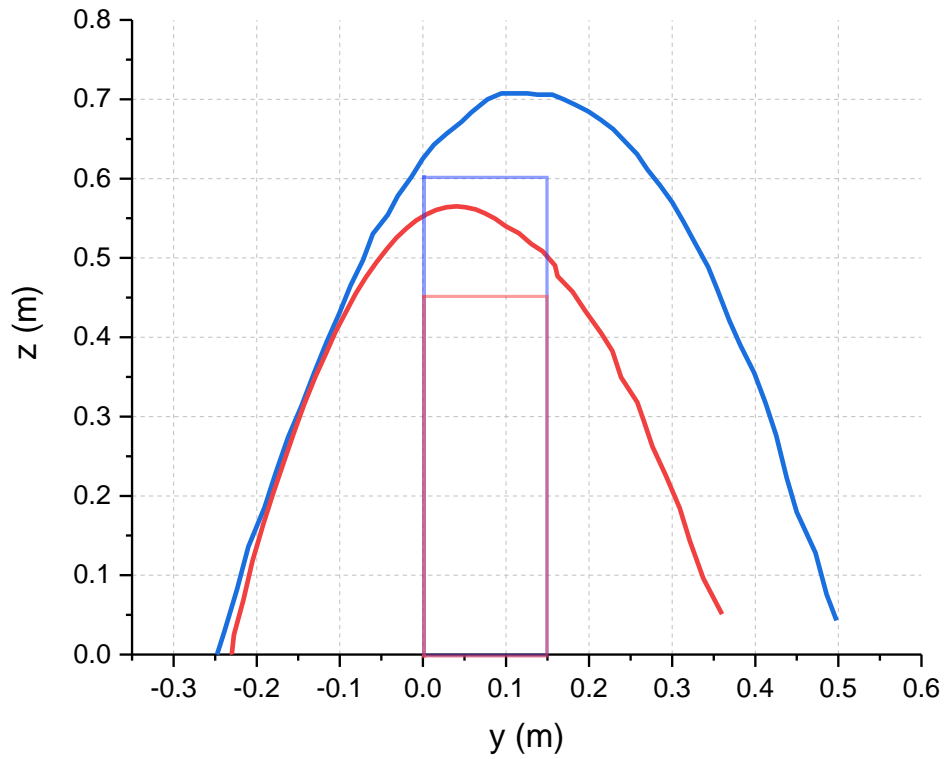


Figure 4.8 Jumping trajectories of overcoming two different obstacles by sensing an obstacle with the distance sensor and the IMU. The height of the red obstacle is 0.45 m, the blue obstacle is 0.6 m, and the distance to both obstacles are about 0.25 m.

Chapter 5. Conclusion

In this thesis, we propose the jumping robot that performs jumping, steering, take-off angle adjustment, and self-righting with only two motors. Jumping and steering shares the motor through jumping/steering gearbox. Self-righting of front side landing shares the motor with take-off angle adjustment, and back side landing shares the mechanism of jumping. By integrating additional functions into one jumping robot, the robot can arrive at the desired location in an unstructured environment. The robot can jump high or low by adjusting the take-off angle depending on the size of the obstacles the robot encounters during its mission. Moreover, by steering, the robot can take a detour around a barrier that it cannot jump over.

A Dynamic model of the jumping robot is established to analyze the motion of the jumping robot. The dynamics is analyzed based on the Lagrangian formulation, including both jumping without slip and jumping with slip which should consider friction force. To estimate the jumping trajectories of the robot with respect to different body angles, the relations between the take-off angle/velocity and the body angle are obtained by simulated results and compared with experimental results. When there is no slip at high body angles, the take-off angle is equal to the body angle, and the take-off velocity is constant with respect to the body angle. When slip occurs at low body angles, the take-off velocity decreases because of the energy

loss due to slip, and the take-off angle is larger than the body angle.

Experimental results show the reachable range of the jumping robot. The robot can change the jumping trajectory between the maximum height and the maximum distance. Also, the robot can steer 360-degree continuously, so it can head toward any desired direction. Jumping on terrain with obstacles demonstrates that integrating additional functions enables the robot to pass the various obstacles. Also, demonstration of sensing the obstacle and determining its trajectory show that it can overcome an obstacle without human intervention.

The jumping robot could be applied to tasks such as planetary exploration, search and rescue, and environmental monitoring. For example, if the multiple robots are deployed, each robot can be one node of the sensor network. Jumping robot can ascend to a high position, therefore, a wider view angle can be obtained when using a camera for reconnaissance. Also, when collaborating with other small-scale robots that have different locomotion modes or different functions, jumping robots could perform tasks which should overcome large obstacles or reach to the top side of the obstacles.

The robot may be improved in the future research, as follows:
(1) it takes the robot too long time to store energy, steer one revolution and self-right. All three functions are performed using the head motor. The motor has a high gear ratio to provide sufficient force, so it has small rpm. Furthermore, the rhombus-shaped structure is good for large energy-storage capacity; however, the

length of the cord to fully compress the jumping linkage is also long. The robot would be more practical if it reduces the time to perform these functions; (2) When landing after jumping, the robot receives a large impact. Therefore, experiments on durability should be performed and further studies about protecting parts from impact are necessary. (3) Performance of each function was examined in flat ground. Further experiments should be performed to confirm that this robot can be used in real unstructured environments.

Bibliography

- [1] I. Paprotny and S. Bergbreiter, “Small-scale robotics: An introduction,” in *workshop at the IEEE International Conference on Robotics and Automation*, pp. 1–15, 2013.
- [2] M. Kaspari and M. D. Weiser, “The size-grain hypothesis and interspecific scaling in ants,” *Functional Ecology*, vol. 13, no. 4, pp. 530–538, 1999.
- [3] M. Kovac, M. Fuchs, A. Guignard, J. Zufferey, and D. Floreano, “A miniature 7g jumping robot,” in *IEEE International Conference on Robotics and Automation*, pp. 373–378, 2008.
- [4] M. Noh, S. -W. Kim, S. An, J. -S. Koh, and K. -J. Cho, “Flea-inspired catapult mechanism for miniature jumping robots,” *IEEE Transactions on Robotics*, vol. 28, no. 5, pp. 1007–1018, Oct. 2012.
- [5] V. Zaitsev, O. Gvirsman, U. B. Hanan, A. Weiss, A. Ayali, and G. Kosa, “A locust-inspired miniature jumping robot,” *Bioinspiration & Biomimetics*, vol. 10, no. 6, p. 066012, Nov. 2015.
- [6] R. Armour, K. Paskins, A. Bowyer, J. Vincent, and W. Megill, “Jumping robots: a biomimetic solution to locomotion across rough terrain,” *Bioinspiration & Biomimetics*, vol. 2, no. 3, pp. S65–S82, Jun. 2007.
- [7] D. W. Haldane, M. Plecnik, J. K. Yim, and R. S. Fearing, “Robotic vertical jumping agility via series-elastic power

- modulation,” *Science Robotics*, vol. 1, no. 1, Dec. 2016.
- [8] F. Li, W. Liu, X. Fu, G. Bonsignori, U. Scarfogliero, C. Stefanini, and P. Dario, “Jumping like an insect: Design and dynamic optimization of a jumping mini robot based on bio-mimetic inspiration,” *Mechatronics*, vol. 22, no. 2, pp. 167–176, Mar. 2012.
- [9] M. Wang, X. -z. Zang, J. -z. Fan, and J. Zhao, “Biological jumping mechanism analysis and modeling for frog robot,” *Journal of Bionic Engineering*, vol. 5, no. 3, pp. 181–188, Sep. 2008.
- [10] A. Yamada, M. Watari, H. Mochiyama, and H. Fujimoto, “An asymmetric robotic catapult based on the closed elastica for jumping robot,” in *IEEE International Conference on Robotics and Automation*, pp. 232–237, 2008.
- [11] G. -P. Jung, C. S. Casares, S. -P. Jung, R. S. Fearing, and K. -J. Cho, “An integrated jumping-crawling robot using height-adjustable jumping module,” in *IEEE International Conference on Robotics and Automation*, pp. 4680–4685, 2016.
- [12] J. Zhao, J. Xu, B. Gao, N. Xi, F. J. Cintron, M. W. Mutka, and Li. Xiao, “MSU Jumper: A single-motor-actuated miniature steerable jumping robot,” *IEEE Transactions on Robotics*, vol. 29, no. 3, pp. 602–614, June 2013.
- [13] P. Fiorini and J. Burdick, “The development of hopping capabilities for small robots,” *Autonomous Robots*, vol. 14, no.

2–3, pp. 239–254, Mar. 2003.

- [14] J. Zhang, G. Song, Y. Li, G. Qiao, A. Song, and A. Wang, “A bio–inspired jumping robot: Modeling, simulation, design, and experimental results,” *Mechatronics*, vol. 23, no. 8, pp. 1123–1140, Dec. 2013.
- [15] M. Kovac, M. Schlegel, J. –C. Zufferey, and D. Floreano, “Steerable miniature jumping robot,” *Autonomous Robots*, vol. 28, no. 3, pp. 295–306, Dec. 2010.
- [16] J. Zhang, X. Yang, G. Song, Y. Zhang, S. Fei, and A. Song, “Structural–parameter–based jumping–height–and–distance adjustment and obstacle sensing of a bio–inspired jumping robot,” *International Journal of Advanced Robotic Systems*, vol. 12, no. 6, p. 66, Jan. 2015.
- [17] K. Chen, D. Chen, Z. Zhang, and M. Wang, “Jumping robot with initial body posture adjustment and a self–righting mechanism,” *International Journal of Advanced Robotic Systems*, vol. 13, no. 3, p. 127, Jan. 2016.
- [18] M. A. Woodward and M. Sitti, “MultiMo–Bat: A biologically inspired integrated jumping–gliding robot,” *The International Journal of Robotics Research*, vol. 33, no. 12, pp. 1511–1529, Oct. 2014.
- [19] S. Yim, S. –M. Baek, G. –P. Jung, and K. –J. Cho, “An omnidirectional jumper with expanded movability via steering, self–righting and take–off angle adjustment,” in *IEEE/RSJ International Conference on Intelligent Robots and Systems*,

pp. 416–421, 2018.

- [20] F. E. Udwadia and R. E. Kalaba, “Nonideal constraints and Lagrangian dynamics,” *Journal of Aerospace Engineering*, vol. 13, no. 1, pp. 17–22, Jan. 2000.
- [21] D. Brown. (2011) [Online]. *Tracker*. Available: <http://physlets.org/tracker/>

방향 전환, 도약 각도 조절, 자세 교정이 가능한 점핑 로봇

도약 로봇은 로봇 자신의 크기보다 큰 장애물을 넘어 이동할 수 있다. 도약 운동만으로 원하는 위치에 도달하기 위해 도달 가능한 범위를 넓힐 수 있는 방향 전환, 도약 각도 조절, 자세 교정 기능이 통합된 점핑 로봇들이 개발됐다. 이 때 추가 기능을 통합하면 로봇의 질량이 증가하고 도약 성능이 감소하므로 질량을 줄이기 위한 설계가 필요하다. 본 논문에서는 방향 전환, 도약 각도 조절, 자세 교정이 가능한 도약 로봇을 제안하며, 도약 성능 감소를 최소화하기 위해 메커니즘과 구동기를 공유할 수 있도록 로봇이 설계되었다. 로봇의 질량은 70.1 g으로 최대 높이 1.02 m, 최대 거리 1.28 m를 도약할 수 있다. 또한, 전 방향으로 도약할 수 있으며, 반복 도약으로 더 먼 곳에 도달할 수 있다. 로봇의 거동을 예측할 수 있는 동역학 모델을 세웠으며, 미끄러짐이 없이 도약하는 경우뿐만 아니라 미끄러짐이 포함된 도약에 대해서도 로봇의 거동을 확인하고 도약 궤적을 계획할 수 있다. 구동기의 수보다 많은 기능의 수를 구현하는 설계 방법은 다른 소형 로봇의 설계에 적용할 수 있을 것이다. 이 로봇은 비정형 환경에서 수색, 정찰 혹은 탐사와 같은 임무를 수행하는 데 활용 가능할 것이다.

주요어 : 이동 로봇, 도약 로봇, 다기능 도약 로봇, 메커니즘 공유,
구동기 공유

학번 : 2017-29144